CHEMISTRY
A EUROPEAN JOURNAL

DOI: 10.1002/chem.200902263

Chemical Dealloying Mechanism of Bimetallic Pt–Co Nanoparticles and Enhancement of Catalytic Activity toward Oxygen Reduction

Feng-Ju Lai,[a] Wei-Nien Su,[a] Loka Subramanyam Sarma,[a] Din-Goa Liu,[b]
Cheng-An Hsieh,[b] Jyh-Fu Lee,[b] and Bing-Joe Hwang*[a, b]

Abstract: The chemical dealloying mechanism of bimetallic Pt–Co nanoparticles (NPs) and enhancement of their electrocatalytic activity towards the oxygen reduction reaction (ORR) have been investigated on a fundamental level by the combination of X-ray absorption spectroscopy (XAS) and aberration-corrected scanning transmission electron microscopy (STEM). Structural parameters, such as coordination numbers, alloy extent, and the unfilled d states of Pt atoms, are derived from the XAS spectra, together with the compositional variation analyzed by line-scanning energy-dispersive X-ray spectroscopy (EDX) on an atomic scale, to gain new insights into the dealloying process of bimetallic Pt–Co NPs. The XAS results on acid-treated Pt–Co/C NPs reveal that the Co–Co bonding in the bimetallic NPs dissolves first and the remaining morphology gradually transforms to a Pt-skin structure. From cyclic voltammetry and mass activity measurements, Pt–Co alloy NPs with a Pt-skin structure significantly enhance the catalytic performance towards the ORR. Further, it is observed that such an imperfect Pt-skin surface feature will collapse due to the penetration of electrolyte into layers underneath and cause further dissolution of Co and the loss of Pt. The electrocatalytic activity decreases accordingly, if the dealloying process lasts for 4 h. The findings not only demonstrate the importance of appropriate treatment of bimetallic catalysts, but also can be referred to other Pt bimetallic alloys with transition metals.

Keywords: catalytic activity · cobalt · nanoparticles · oxygen reduction reaction · platinum

Introduction

Proton exchange membrane fuel cells (PEMFCs) have been developed as an alternative power source for various portable and stationary applications due to their low emission, convenient operation at low temperature, and high energy efficiency.[1–4] At the cathode of a PEMFC, oxygen molecules react with the protons permeating through the membrane to form water on a Pt or Pt alloy catalyst. The electroreduction of oxygen on the cathode in acidic solutions is always a slow reaction. The overpotential phenomena and significant power losses[5] reduce the overall energy efficiency of PEMFCs. Concerns like reducing the usage of noble metals have been considered to be major challenges in promoting the technology. To overcome such issues, some studies have reported that Pt-based alloys with transition metals (Co,[6] Ni,[7] Cr,[8] etc.) are helpful to improve the kinetics of the oxygen reduction reaction (ORR).[9,10] A number of explanations have been given for the observed improvement in activity by alloying Pt with a less noble metal. The benefits include a lower oxidation state of the Pt, which can suppress the formation of Pt oxide,[11,12] a shorter Pt–Pt interatomic distance, a more favorable absorption of O_2 due to the geometric effect,[13,14] increased 5d orbital vacancies (electronic effect), and the formation of a thin Pt skin on the surface of the alloy. It was demonstrated that the formation of Pt-skin alloys is caused by the dissolution of the base metal from Pt alloy under acidic conditions.[6,8,15–19] Stamenkovic et al.[19–21] have shown that the polycrystalline Pt_3Co nanocrystal with a Pt-skin layer is more active than the polycrystalline Pt and bimetallic Pt_3M surfaces (M = Fe, Ni, V, and Ti), because of the unusual electronic properties of the

---

[a] F.-J. Lai, W.-N. Su, Dr. L. S. Sarma, Prof. Dr. B.-J. Hwang
Department of Chemical Engineering
National Taiwan University of Science and Technology
#43, Sec.4, Keelung Rd., Taipei 10607 (Taiwan)
Fax: (+886) 2-27376644
E-mail: bjh@mail.ntust.edu.tw

[b] D.-G. Liu, C.-A. Hsieh, Dr. J.-F. Lee, Prof. Dr. B.-J. Hwang
National Synchrotron Radiation Research Center
Hsinchu 30076 (Taiwan)
Fax: (+886) 3-5783813

Pt_3Co nanocrystal. Strasser and Koh[22] have reported that the catalytic activity of the bimetallic nanoparticles is strongly influenced by the degree of voltammetric surface dealloying. Chen et al.[23] attempted to correlate surface atomic structures and near-surface chemical compositions that govern activity. They suggested that by creating a percolated structure with Pt-rich and Pt-poor regions within individual Pt_3Co nanoparticles through acid treatment, their ORR activity could be increased by up to two orders of magnitude when compared to Pt nanoparticles.

The performance of PEMFCs is also influenced by several other factors, such as electrochemical reaction conditions, dissolution of cathode materials, and degradation of electrolyte.[24–26] Watanabe et al.[27] analyzed the ordered and disordered structure of Pt–Co catalysts by a corrosion test in a phosphoric acid fuel cell (PAFC). A Pt-skin surface feature would be left behind during the course of corrosion, and the dealloying process would be more serious for the ordered structure than the disordered one. It was also found that the content of platinum did not change after 50 h of corrosion measured by energy-dispersive X-ray spectroscopy (EDX) analysis. Gasteiger et al.[28] indicated that the surface-area loss in platinum at high potential was caused by the dissolution of platinum. In another interesting study, Zignani et al.[24] studied the durability of Pt–Co/C and Pt/C catalysts in PEMFCs. The catalytic activity of the bimetallic compound degraded after repetitive cycling for 30 h in sulfuric acid. The dissolution of platinum was detected by inductively coupled plasma–atomic absorption spectroscopy (ICP-AAS) analysis performed on the freshly degraded solution. Even though tools such as EDX, electrochemical analysis, and ICP-AAS could give information on the dissolution of Pt, the morphological transformation has not yet been addressed.

In addition, it is equally important to know the atomic distribution and alloy extent of participating elements in individual bimetallic nanoparticles, because these factors also influence the intrinsic catalytic activity toward the targeted reaction. Furthermore, a fundamental understanding between the ORR activity and nanoparticle structure is necessary to develop inexpensive, stable, and catalytically active materials for the ORR. Although a significant number of experimental and theoretical research efforts have been focused on the influence of the surface chemistry and electronic structure of Pt-alloy single-crystal surfaces, exploration of nanoparticle catalysts requires precise determination of the structure and development of various characterization methodologies.

Aberration-corrected scanning transmission electron microscopy (STEM) in conjunction with the line-scan analysis of atomic-scale EDX could provide insight into the change of surface composition, especially on the edge of a particle's cross-sectional profile.[29–31] The X-ray absorption spectroscopy (XAS) technique can provide morphological information about objects of interest, as well as the distribution of the different species inside the nanoparticles, for example, core–surface segregation.[32] In general, XAS studies can be divided into two parts. One is the X-ray absorption near-edge structure (XANES) region, conventionally from below the edge up to ~30–50 eV. It provides information about the oxidation state and fractional change of d-electron density, as well as the electronic environment of the absorbing atoms. The other is the extended X-ray absorption fine structure (EXAFS) region, extended above the edge up to ~30–1000 eV. EXAFS allows investigations on the short-range ordering and provides geometric information. It gives the number, type, and distance of the backscattering atom surrounding the central absorbing atom.

Herein, we propose a chemical dealloying mechanism for Pt–Co bimetallic alloys and establish its relationship with the catalytic activity toward oxygen reduction through electrochemical analysis. The morphological transformations, and structural and compositional variations of bimetallic Pt–Co nanoparticles in the course of the dealloying process were characterized by the combination of the aforementioned analytical techniques.

Results and Discussion

The Co K-edge XANES spectra measured at various chemical dealloying times are shown in Figure 1. The absorption at 7709 eV corresponds to a 1s to 3d electronic transition of Co metal[33] and the absorption hump at 7725 eV corresponds to a 1s to 4d transition of a cobalt foil.[6] The intensities of the absorption humps from different samples are higher than those of cobalt foil for various chemical dealloying times, which might result from the nanosize effect or the presence of a Co oxide. The Co K-edge Fourier transform (FT) EXAFS spectra are plotted in Figure 2, in which the peaks at 2.5 and 2.7 Å correspond to the Co–Co and Co–Pt first shell coordination, respectively. Furthermore, if Co oxide exists, a peak at 1.9 Å should normally appear in the

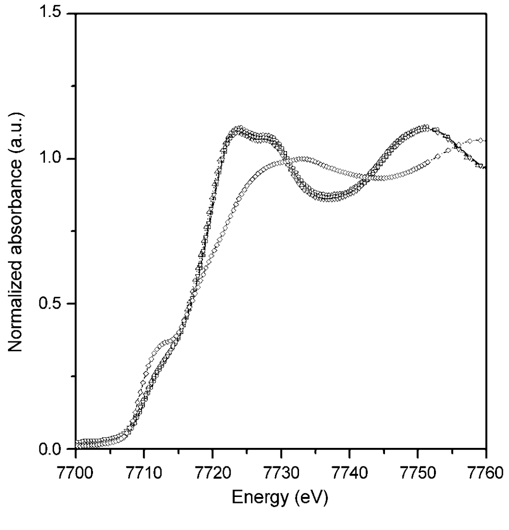

Figure 1. Co K-edge XANES spectra of 30 % Pt–Co/C at different chemical dealloying times (□: initial step (*t* = 0 min), ○: *t* = 15 min, △: *t* = 2 h, ▽: *t* = 4 h, ◇: Co foil).

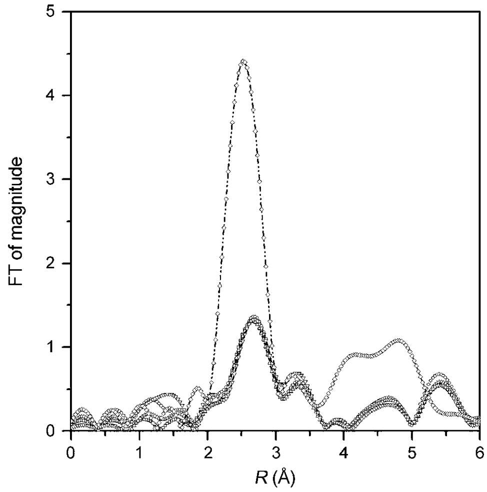

Figure 2. FT-EXAFS spectra at the Co K-edge at different chemical dealloying times (□: initial step ($t=0$ min), ○: $t=15$ min, △: $t=2$ h, ▽: $t=4$ h, ◇: Co foil).

FT-EXAFS spectra. However, the results in Figure 2 clearly confirm the absence of Co oxide in Pt–Co/C nanoparticles at various chemical dealloying times.

The Pt L_{III}-edge XANES spectra measured at different chemical dealloying times are shown in Figure 3. The absorption at 11 564 eV corresponds to $2p_{3/2}$ to 5d electronic transition of Pt metal and the magnitude of the absorption hump is known as the white line,[34,35] which reflects the orbital occupancy of the 5d electronic state. The intensity of the white line should increase with decreasing occupancy in the 5d orbital. Figure 3 shows that the white-line intensities for all samples are lower than that of a Pt foil (see inset). This could be caused by alloying of Co with Pt leading to a high electron density around Pt atoms, and thus the Pt d-band vacancy is decreased. The Pt L_{III}-edge FT-EXAFS spectra at the various chemical dealloying times are depicted in Figure 4, in which the peaks corresponding to the first Pt–Co and Pt–Pt coordination shells appeared at 2.7 Å.

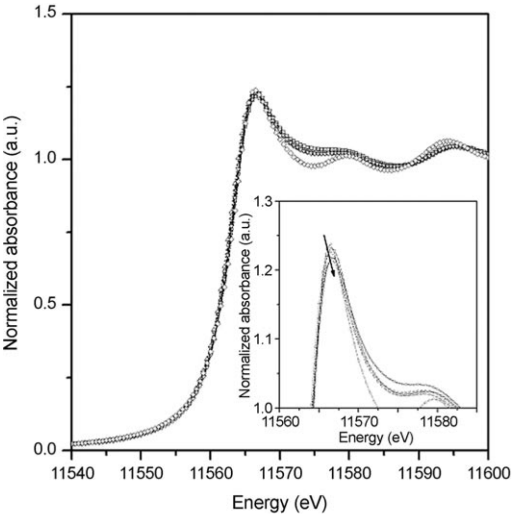

Figure 3. Pt L_{III}-edge XANES spectra at different chemical dealloying times. Inset: the enlarged Pt L_{III}-edge XANES spectra (□: initial step ($t=0$ min), ○: $t=15$ min, △: $t=2$ h, ▽: $t=4$ h, ◇: Pt foil).

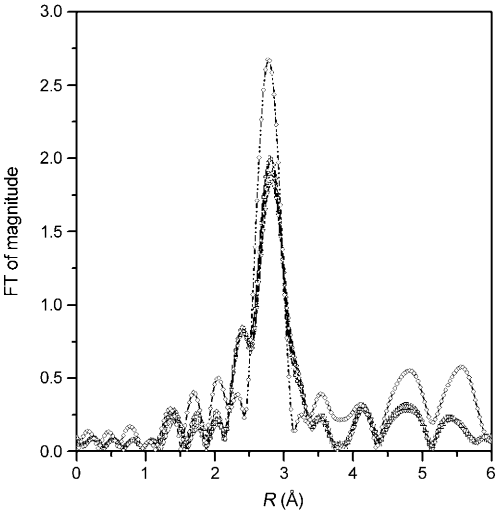

Figure 4. FT-EXAFS spectra at the Pt L_{III}-edge at different chemical dealloying times (□: initial step ($t=0$ min), ○: $t=15$ min, △: $t=2$ h, ▽: $t=4$ h, ◇: Pt foil).

The best-fitting parameters of Co absorbing atoms calculated from the Co K-edge and Pt L_{III}-edge EXAFS spectra at various chemical dealloying times are summarized in Table 1. Before chemical dealloying begins, the coordination number of the Co–Co is 2.4 and the heterometallic coordination of the Co–Pt is found to be 7.0. The corresponding bond lengths are 2.512 and 2.705 Å, respectively. From the Pt L_{III}-edge EXAFS spectra, the coordination numbers for Pt–Co and Pt–Pt are calculated to be 2.7 and 8.8, respectively. The corresponding bond lengths are 2.705 and 2.722 Å, respectively. Similarly, the best-fitting parameters of Pt absorbing atoms obtained from the Co K-edge and Pt L_{III}-edge EXAFS spectra at various chemical dealloying times are listed in Table 2. The total coordination numbers for Co and Pt absorbing atoms can be obtained from $\Sigma N_{\text{Co–}i}$ ($=N_{\text{Co–Pt}}+N_{\text{Co–Co}}$) and $\Sigma N_{\text{Pt–}i}$ ($=N_{\text{Pt–Pt}}+N_{\text{Pt–Co}}$) separately. Before chemical dealloying starts, $\Sigma N_{\text{Pt–}i}$ is larger than $\Sigma N_{\text{Co–}i}$, which indicates that the commercial Pt–Co nanoparticles have a Co-rich shell and Pt-rich core structure, since atoms present on the surface have fewer neighbors than those in the core.[32]

After chemical dealloying for 15 min, the homometallic coordination number of Co ($N_{\text{Co–Co}}$) reduces considerably to 0.4, whereas the heterometallic bonding ($N_{\text{Co–Pt}}$) increases slightly to 9.1. The corresponding bond lengths $R_{\text{Co–Co}}$ and $R_{\text{Co–Pt}}$ are found to be 2.512 and 2.706 Å, respectively. The decrease in the Co–Co coordination number after chemical dealloying implies that there are generally fewer Co atoms neighboring a Co atom. Similarly, the coordination numbers

Table 1. Best-fit parameters of Co absorbing atoms obtained from the analysis of the Co K-edge and Pt L_{III}-edge EXAFS spectra at different chemical dealloying times.

Chemical dealloying time t	Shell	N[a]	R_j[b] [Å]	σ_j^2 ($\times10^{-3}$)[c] [Å^2]	ΔE_0[d] [eV]	R factor[e]
initial step (0 min)	Co–Co	2.4 (±0.6)	2.512 (±0.025)	6.0 (±3.3)	−12.3	0.009
	Co–Pt	7.0 (±0.7)	2.705 (±0.008)	7.3 (±1.0)	5.1	
15 min	Co–Co	0.4 (±0.2)	2.512 (±0.041)	4.9 (±2.8)	−9.6	0.019
	Co–Pt	9.1 (±0.4)	2.706 (±0.007)	7.8 (±1.0)	2.8	
2 h	Co–Pt	9.3 (±0.4)	2.704 (±0.006)	6.8 (±0.8)	2.8	0.010
4 h	Co–Pt	5.2 (±0.3)	2.702 (±0.005)	1.7 (±0.6)	3.5	0.027

[a] N: coordination number. [b] R_j: coordination distance. [c] σ_j^2: a mean squared disorder for the bond distance. [d] ΔE_0: inner potential correction. [e] R factor: residual error.

Table 2. Best-fit parameters of Pt absorbing atoms obtained from the analysis of the Pt L_{III}-edge and Co K-edge EXAFS spectra at different chemical dealloying times.

Chemical dealloying time t	Shell	N[a]	R_j[b] [Å]	σ_j^2 ($\times10^{-3}$)[c] [Å^2]	ΔE_0[d] [eV]	R factor[e]
initial step (0 min)	Pt–Co	2.7 (±0.1)	2.705 (±0.003)	7.3 (±0.3)	7.8	0.009
	Pt–Pt	8.8 (±0.2)	2.722 (±0.001)	5.7 (±0.1)	3.1	
15 min	Pt–Co	2.6 (±0.1)	2.706 (±0.003)	7.8 (±0.3)	7.3	0.019
	Pt–Pt	8.8 (±0.1)	2.723 (±0.001)	5.3 (±0.1)	1.0	
2 h	Pt–Co	2.5 (±0.1)	2.704 (±0.006)	7.8 (±0.7)	8.0	0.010
	Pt–Pt	8.8 (±0.2)	2.724 (±0.002)	5.5 (±0.1)	0.6	
4 h	Pt–Co	1.4 (±0.1)	2.702 (±0.007)	4.0 (±0.6)	8.2	0.027
	Pt–Pt	10.3 (±0.3)	2.726 (±0.002)	6.4 (±0.2)	0.8	

[a] N: coordination number. [b] R_j: coordination distance. [c] σ_j^2: a mean squared disorder for the bond distance. [d] ΔE_0: inner potential correction. [e] R factor: residual error.

for Pt–Co and Pt–Pt are found to be 2.6 and 8.8, respectively. When the chemical dealloying continues for 2 h, the coordination number of the Co–Pt is 9.3 and the bond length is 2.704 Å, whereas the structural parameters of Co–Co are no longer detectable. On the other hand, the coordination numbers of Pt–Co and Pt–Pt are 2.5 and 8.8, with corresponding bond lengths of 2.704 and 2.724 Å, respectively. The increase in coordination number of Co–Pt bonding indicates that the dissolution of the surface Co takes place faster than that of an underneath Co atom and the Co–Pt bonding is more resistant to the dissolution than the Co–Co bonding. The number of platinum atoms exposed to the outer surface of nanoparticles will increase due to the dissolution of the surface Co. Based on the EXAFS spectral analysis, it is observed that Co dissolves gradually thus indicating that Pt–Co nanoparticles have undergone a structural transformation. It is supposed that a surface feature such as a Pt skin might be present during the chemical dealloying process. When the chemical dealloying continues for 4 h, the coordination number of Co–Pt drops to 5.2 with a bond length of 2.702 Å. This implies that the number of platinum atoms surrounding a cobalt atom decreases and the Pt skin might have collapsed. At this stage, the coordination numbers of Pt–Co and Pt–Pt are 1.4 and 10.3, respectively. The corresponding bond lengths are 2.702 and 2.726 Å, respectively.

To quantify differences in the white-line intensity between the catalyst and a reference platinum foil, a method originally developed by Mansour et al.[36] and later modified by Reifsnyder et al.[37] was adopted. The fractional change in the total number of unfilled d states (f_d) of the sample compared to the number in the reference foil can be formulated as Equation (1):

$$f_{\rm d} = \frac{\Delta A \sigma_3 + 1.11\ \Delta A_2 \sigma_2}{A_{3r}\sigma_3 + 1.11\ A_{2r}\sigma_2} \qquad (1)$$

After subtracting the platinum foil data from the catalyst data, the resulting curves were then numerically integrated between −10 and 14 eV for both the $L_{II}(\Delta A_2)$- and $L_{III}(\Delta A_3)$-edge. The areas are normalized by multiplying with the X-ray absorption cross section at the edge jump (σ). Values of 117.1 and 54.2 cm^{2}g^{-1} were used for the absorption cross section at the platinum L_{III}- and L_{II}-edges, respectively. If the number of unfilled d states in the reference material ($h_{\rm Tr}$) is known, the number of unfilled d states in the sample ($h_{\rm Ts}$) can then be calculated by Equation (2):

$$h_{\rm Ts} = (1 + f_{\rm d})\, h_{\rm Tr} \qquad (2)$$

Figure 5 gives the unfilled d states of Pt in the Pt–Co nanoparticles calculated at different chemical dealloying times. The number of unfilled d states relates to factors such as morphology, particle size,[38] and alloy extent. When the chemical dealloying process starts, the bonding of Co–Co starts to dissolve (see Table 1). The particle size will de-

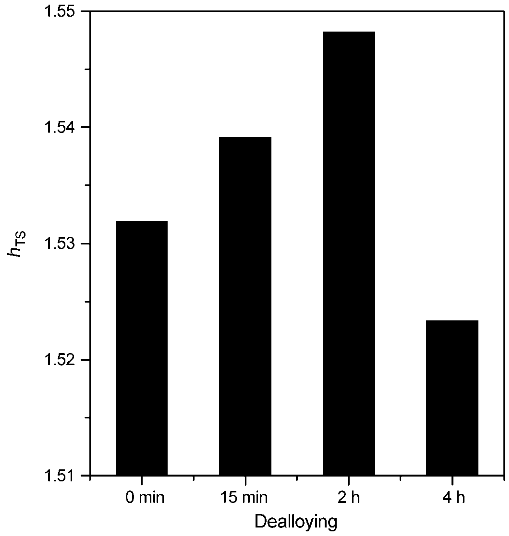

Figure 5. Calculated unfilled Pt d states ($h_{\rm Ts}$) of Pt–Co bimetallic nanoparticles obtained from XANES data at different chemical dealloying times.

crease in the course of chemical dealloying (see Table 3), and the coordination number of Co–Pt bonding increases in the 2 h of chemical dealloying. Consequently, the number of unfilled d states of Pt increases due to the smaller particle size and it becomes a Pt-rich surface. After chemical dealloying for 4 h, the number of unfilled d states of the surface platinum drops and is lower than the value at 2 h. The decrease in unfilled d states of surface Pt at 4 h could be caused by a significant morphological change, such as collapse of the Pt skin.

Table 3. Bulk composition and particle size of Pt–Co nanoparticles during the chemical dealloying process.

Chemical dealloying time *t*	X_{Co}/X_{Pt}	X_{Pt}	X_{Co}	Particle size [nm] (from TEM)
initial step (0 min)	0.39	0.720	0.280	6–7
15 min	0.29	0.774	0.226	6–7
2 h	0.27	0.784	0.216	5–6
4 h	0.27	0.784	0.216	4–5

The molar ratio X_{Co}/X_{Pt} of the bulk sample can be derived from the edge jumps of the Co K-edge and Pt L_{III}-edge in the XANES spectra shown in Figure 1 and Figure 3, respectively. When the chemical dealloying begins, the molar ratio X_{Co}/X_{Pt} is found to be 0.39. After chemical dealloying for 15 min, the molar ratio decreases greatly, as shown in Table 3. This suggests that cobalt dissolves into the sulfuric acid solution. When the chemical dealloying continues for 4 h, the molar ratio X_{Co}/X_{Pt} remains almost the same as the value observed at 2 h. It is noted that the measurements only revealed the bulk composition of samples, but the actual surface composition on the nanoparticles' surface might have changed. In the course of corrosion, the size of the nanoparticles observed by TEM becomes smaller, and its distribution remains quite uniform from the TEM data at different chemical dealloying steps. As cobalt dissolves, less cobalt exists on the surface of the Pt–Co nanoparticles. The morphology left behind might be similar to a Pt skin.[6,8,15–19]

The aberration-corrected high-angle annular dark-field (HAADF) images recorded using an FEI-TEM 2000 microscope and STEM in conjunction with the line-scan analysis of atomic-scale EDX revealed the compositional variation in the course of chemical dealloying. Due to the nature of EDX, the signal collected from the outermost part of scanned nanoparticles is less influenced by other neighboring and inner atoms and is worthy of more attention. The edges of the particle can be observed from cross-sectional composition profiles by EDX line scanning.[29–31] The high-resolution TEM (HRTEM) image of the Pt–Co system before the corrosion is given in Figure 6a and the cross-sectional compositional line profiles detected by EDX are shown in Figure 6b. The circle and square lines represent smoothed compositional profiles for the Co K-edge and Pt L_{III}-edge, respectively. The results show that cobalt generally exhibits a higher intensity than platinum, especially at edges.

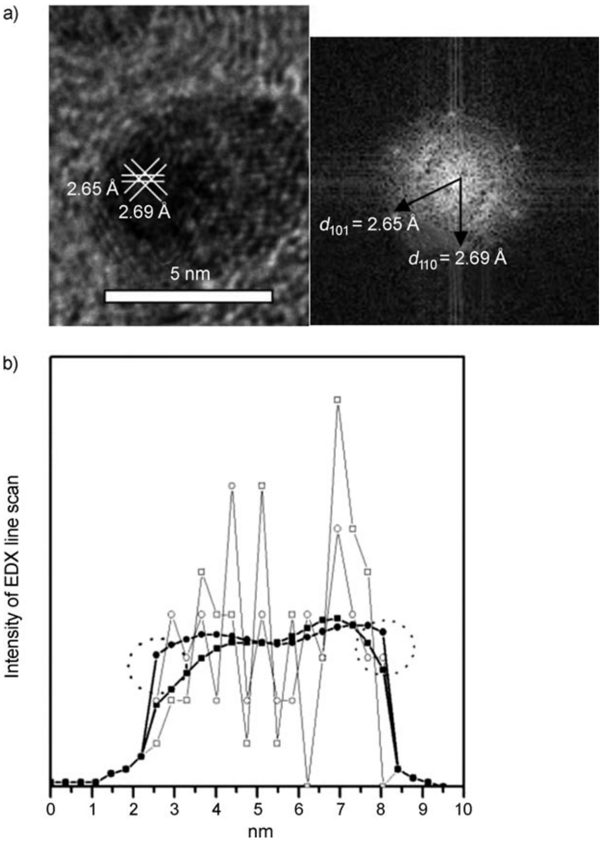

Figure 6. a) HRTEM image of the Pt–Co system at the initial step of chemical dealloying; b) cross-sectional compositional line profile taken from the nanoparticle (□: Pt M-edge, ■: Pt M-edge (smooth), ○: Co K-edge, ●: Co K-edge (smooth)).

This observation indicates that the intrinsic structure of the Pt–Co nanoparticle has a surface enriched with Co and the result is consistent with the aforementioned EXAFS spectral analysis.

The HRTEM image and cross-sectional compositional profiles of Pt–Co nanoparticles exposed to the chemical dealloying for 2 h are shown in Figure 7a and b. When dealloying continues for 2 h, Pt becomes dominant in the surface of the specimen, as realized from the EDX measurements shown in Figure 7b, in which the Pt profile has a much higher intensity than that of Co. These observations indicate that the Pt–Co alloy nanoparticles exhibit a Pt-skin structure at this stage. The HRTEM image and cross-sectional compositional profiles of Pt–Co nanoparticles exposed to the chemical dealloying for 4 h are presented in Figure 8a and b. Interestingly, the intensity of platinum decreases significantly after 4 h of dealloying, as shown in Figure 8b. This finding implies that the Pt-skin surface feature is strongly influenced by the continuous corrosion and becomes fragile. Some of the characteristic features are finally destroyed.

XAS appears to be a suitable technique to solve the three-dimensional structure of both mono- and bimetallic nanoparticles. Recently, we explored several parameters from the X-ray absorption data required for the quantitative

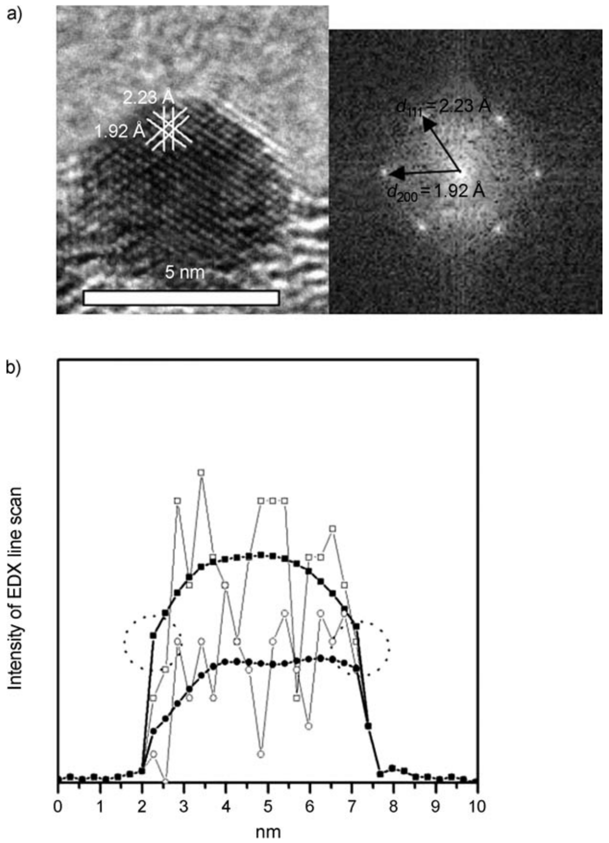

Figure 7. a) HRTEM image of a Pt–Co nanoparticle taken at 2 h of chemical dealloying; b) cross-sectional compositional line profile taken from the nanoparticle (□: Pt M-edge, ■: Pt M-edge (smooth), ○: Co K-edge, ●: Co K-edge (smooth)).

characterization of the structure of bimetallic nanoparticles.[32] In general, P_{observed} ($=N_{\text{Pt–Co}}/\Sigma N_{\text{Pt–}i}$) can be represented as the ratio of the scattering "Co" atom coordination number around absorbing "Pt" atoms ($N_{\text{Pt–Co}}$) to the total coordination number of absorbing atoms ($\Sigma N_{\text{Pt–}i}=N_{\text{Pt–Co}}+N_{\text{Pt–Pt}}$). The parameter P_{observed} provides quantitative information on the probability that a Pt atom bonds with a Co atom. In other words, it represents the Pt distribution in the nanoparticles. Similarly, R_{observed} ($=N_{\text{Co–Pt}}/\Sigma N_{\text{Co–}i}$) can be represented as the ratio of the scattering "Pt" atom coordination number around absorbing "Co" atoms ($N_{\text{Co–Pt}}$) to the total coordination number of absorbing atoms ($\Sigma N_{\text{Co–}i}=N_{\text{Co–Co}}+N_{\text{Co–Pt}}$). The parameter R_{observed} provides quantitative information on probability that a Co atom bonds with a Pt atom. In other words, it represents the Co distribution in the nanoparticles. Once P_{observed} and R_{observed} are known, the extent of Pt alloying (J_{Pt}) and Co alloying (J_{Co}) in the Pt–Co bimetallic nanoparticle can be conveniently estimated by Equations (3) and (4), respectively:

$$J_{\text{Pt}} = P_{\text{observed}}/P_{\text{random}} \times 100\,\% \tag{3}$$

$$J_{\text{Co}} = R_{\text{observed}}/R_{\text{random}} \times 100\,\% \tag{4}$$

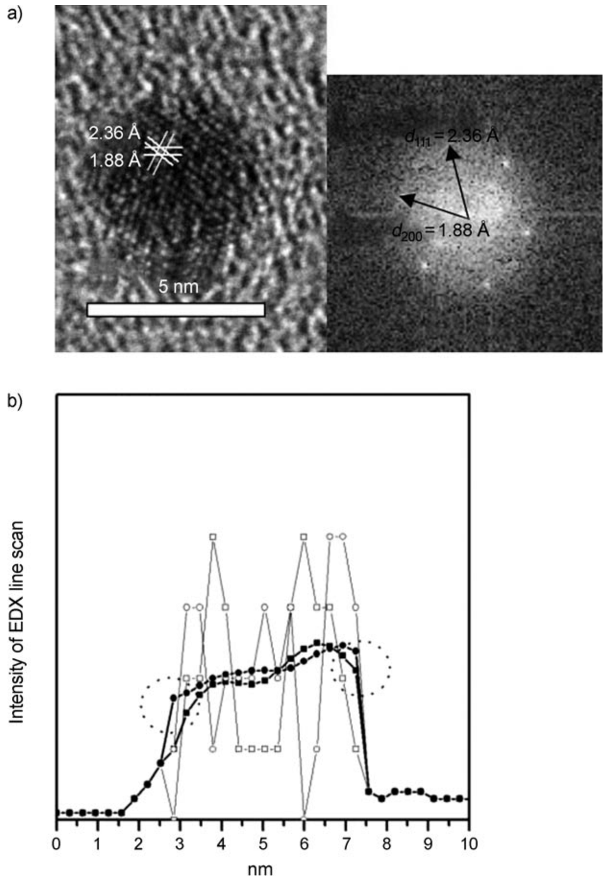

Figure 8. a) HRTEM image of a Pt–Co nanoparticle taken at 4 h of chemical dealloying; b) cross-sectional compositional line profile taken from the nanoparticle (□: Pt M-edge, ■: Pt M-edge (smooth), ○: Co K-edge, ●: Co K-edge (smooth)).

The parameters P_{random} and R_{random} are the ratios calculated for perfectly alloyed bimetallic nanoparticles. They can be derived from the molar ratios of Co and Pt in Pt–Co bimetallic nanoparticles, as represented in Table 3.

During the XAS data fit, the following constraint was imposed on the heterometallic bonds, in which X_{M} is the molar ratio of the metal [Eq. (5)]:

$$N_{\text{Pt–Co}} = (X_{\text{Co}}/X_{\text{Pt}}) \times N_{\text{Co–Pt}} \tag{5}$$

In addition to total coordination numbers $\Sigma N_{\text{Pt–}i}$ and $\Sigma N_{\text{Co–}i}$, the introduced structural parameters P_{observed} and R_{observed} as well as J_{Pt} and J_{Co} can be deduced accordingly and are presented in Table 4. In general, the lower the J_i value, the more serious is the segregation of "i" atoms in nanoparticles (here i means either Pt or Co). In the present study, the bonding of Co–Co is dissolved first while the coordination number of Co–Pt bonding is increased. After Pt–Co nanoparticles are exposed to chemical dealloying for 2 h, the alloy extent of Co (J_{Co}) increases with increasing J_{Pt} and this observation indicates well-scattered Pt and Co atoms in Pt–Co nanoparticles. This ensures a better catalytic performance in the ORR. In contrast, inferior ORR performance can be anticipated if J_{Pt} decreases.

Table 4. Total coordination numbers and alloy extent for Pt and Co estimated from EXAFS spectra during the chemical dealloying process.

Chemical dealloying time t	ΣN_{Pt-i}	ΣN_{Co-i}	P_{obsd}	R_{obsd}	J_{Pt} [%]	J_{Co} [%]
initial step (0 min)	11.5 (±0.3)	9.5 (±1.3)	0.24 (±0.01)	0.74 (±0.07)	85 (±4)	103 (±10)
15 min	11.4 (±0.2)	9.5 (±0.6)	0.23 (±0.01)	0.96 (±0.04)	101 (±4)	124 (±5)
2 h	11.3 (±0.3)	9.3 (±0.4)	0.23 (±0.01)	1.00 (±0.04)	104 (±5)	127 (±5)
4 h	11.7 (±0.4)	5.2 (±0.3)	0.12 (±0.01)	1.00 (±0.06)	56 (±5)	128 (±8)

Although the measurements and calculations from EXAFS and EDX offered some insights into the morphological transformation during the chemical dealloying process, the findings require further evidence about the electrochemical properties of Pt–Co nanoparticles. To this end, cyclic voltammetry of Pt–Co/C catalysts exposed to different chemical dealloying times in 0.5 M sulfuric acid solution was conducted at a scan rate of 5 mV s^{-1} (cyclic voltammetry not shown here). From the measured cyclic voltammograms, the surface area of Pt can be calculated from the hydrogen desorption peaks. Under the same loading of Pt, different hydrogen desorption peaks are observed for various chemical dealloying times representing different surface areas of these catalysts, as shown in Table 5. The measured surface area of Pt decreases significantly from 2 to 4 h and it shows that the Pt-skin structure might have collapsed due to the effect of chemical dealloying.[39]

Table 5. Surface area calculation from hydrogen desorption peaks of cyclic voltammetry during the chemical dealloying process.

Chemical dealloying time t	Initial step (0 min)	15 min	2 h	4 h
surface area [m^2 g^{-1}]	11.05	11.09	15.82	12.54

Hydrodynamic voltammograms recorded at 1 mV s^{-1} for the ORR at different chemical dealloying times are shown in Figure 9. The ORR under the potential 0.7 V is diffusion-controlled, and is under a mixed region of diffusion–kinetic control from 0.7 to 0.85 V. The region higher than 0.85 V is kinetically controlled. As can be seen in Figure 9, the ORR activity differs significantly, and the Pt–Co nanoparticles exhibit a better catalytic performance after 2 h of chemical dealloying and a positive shift of 17.3 mV in half-wave potential relative to the initial step. However, after 4 h of chemical dealloying, the cyclic voltammogram and ORR activity show an inferior function of the catalyst.

Figure 10 shows the mass activity of Pt–Co catalyst measured at 0.9 V. The mass activity increases considerably at a dealloying time of 2 h and it decreases after 4 h. When the catalyst is corroded in acid, the morphology of the Pt–Co nanoparticles gradually changes due to the dissolution of Co. While the corrosion proceeds, Pt remains on the surface of the bimetallic catalyst and it becomes a “jagged” Pt skin. This feature enables better utilization of Pt because more Pt atoms are exposed to the outer surface and the active surface area increases. Accordingly, the electrocatalytic performance for ORR increases significantly. The results reported in Table 4 show that the higher alloy extent of Pt–Co nanoparticles favors the ORR efficiency. The results from cyclic voltammograms and mass activity agree with the variations in J_{Co} and J_{Pt} mentioned in the previous section. The better ORR performance is retained as long as the Pt-skin structure is stable; however, once the Pt-skin structure breaks (after chemical dealloying for 4 h), the catalytic performance drops accordingly.

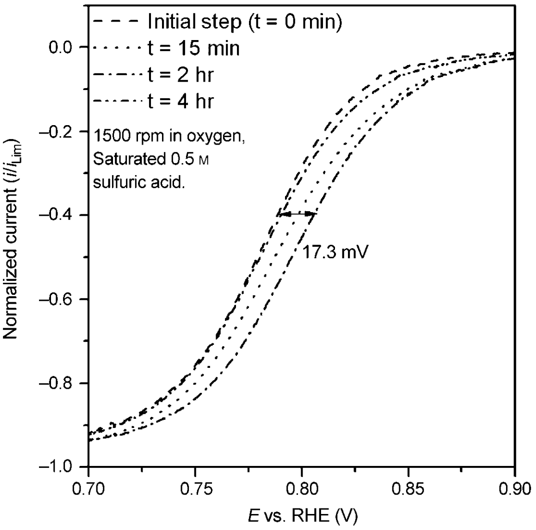

Figure 9. Hydrodynamic voltammograms recorded at 1 mV s^{-1} for the ORR at different chemical dealloying times. RHE: reversible hydrogen electrode.

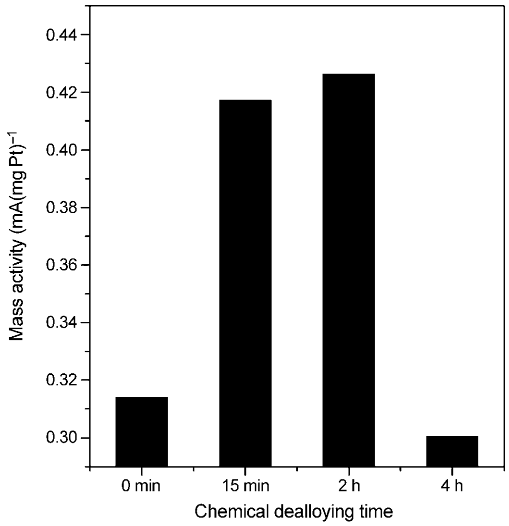

Figure 10. Mass activity measured at 0.9 V (reversible hydrogen electrode, RHE) at different chemical dealloying times.

By summarizing the results from the XAS spectral analysis, EDX line scanning, and electrochemical analyses, a plau-

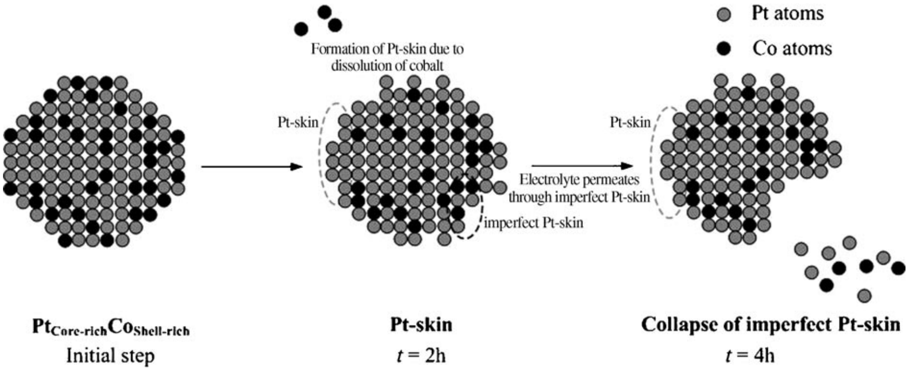

Figure 11. Schematic representation of structural changes of Pt–Co bimetallic nanoparticles at various times of the chemical dealloying process.

sible explanation of the chemical dealloying mechanism for Pt–Co nanoparticles is proposed and is shown in Figure 11. It shows how the morphology of Pt–Co nanoparticles evolves from a Pt-rich core/Co-rich shell structure in the course of the chemical dealloying process. The characteristic Pt-skin feature exhibits a better catalytic performance and will also be damaged if chemical dealloying lasts too long. The existence of vacancies, tunnels, or perhaps voids in the clusters results in an imperfect skin. We believe that during the chemical dealloying process electrolyte passes through the imperfect Pt skin into layers underneath and dissolves cobalt consequently. This finally causes the collapse of the imperfect Pt skin. Proper annealing enables the modification of the imperfect Pt skin, which may improve the catalytic activity and stability.[22,40] These findings demonstrate the importance of appropriate treatment and could apply to other Pt bimetallic alloys associated with transition metals.

Conclusion

The structural transformation of a commercially available Pt–Co catalyst was studied under chemical dealloying conditions in sulfuric acid for different periods of time. The variations in morphology, composition, structure, and electrochemical activity were characterized by EXAFS, STEM of the EDX line scans, and electrochemical analyses. In addition, the unfilled Pt d states of the bimetallic catalyst were calculated from the XANES data. The Pt–Co nanoparticles initially exhibit a Co-rich shell and Pt-rich core structure. As the chemical dealloying proceeds, the Co–Co bonding dissolves gradually, which results in smaller nanoparticles having a rough, imperfect Pt skin with sculpted shapes. Electrochemical measurements show that Pt–Co nanoparticles have a superior catalytic performance for the ORR and higher activity after dealloying for 2 h. When the chemical dealloying continues for 4 h, the electrolyte penetrating into the imperfect Pt skin dissolves cobalt present in layers underneath, and the surface feature of the nanoparticles finally collapses. Suitable annealing conditions may improve the stability and durability of the imperfect Pt skin. A mechanism of the structural variations has been proposed and the experimental results show good agreement with analytical ones. The findings not only demonstrate the importance of appropriate treatment of catalysts, but also can be referred to other Pt bimetallic alloys with transition metals. We believe that by properly employing the chemical dealloying technique, it can be further used to create a Pt skin in other Pt bi- or multimetallic alloys to enhance the electrocatalytic performance for the ORR.

Experimental Section

Sample preparation: A commercial catalyst powder of carbon-supported 30 wt % Pt–Co (1:1 a/o) made by BASF/Etek was selected. Pt–Co was subjected to an acid treatment by immersing the Pt–Co/C powder (0.4 g) in 0.5 M sulfuric acid solution and stirring for 15 min, 2 h, or 4 h. The solubility of cobalt sulfate hydrate is 36.2 g per 100 mL at 20 °C. Even if cobalt in the nanoclusters were fully dissolved in electrolyte, Co saturation would not occur during the chemical dealloying process. After that, samples were cleaned with deionized water to remove any residual sulfuric acid. The sample was then dried and subjected to heat treatment at 300 °C under an atmosphere of 10 % H_2 and 90 % N_2 for 1 h to remove surface oxides if present.

TEM measurements: HRTEM examination was performed on an FEI Tecnai G 20 microscope that was operated at an accelerating voltage of 200 kV. Specimens were prepared by ultrasonically dispersing a known amount of catalyst powder in toluene, placing a drop on the copper grid, and drying in an oven.

XAS measurements: X-ray absorption spectra were recorded at beam line 17C, National Synchrotron Radiation Research Center, Taiwan. The electron storage ring was operated at 1.5 GeV with a current of 300 mA. A Si(111) double-crystal monochromator was employed for energy selection with a resolution $\Delta E/E$ better than 2×10^{-4} at both the Pt L_{III}-edge (11 564 eV) and the Co K-edge (7709 eV). All experiments on bimetallic nanoparticles were conducted in a purpose-made cell of stainless steel for powder XAS study. One hole was made in the cell. After placing the solid samples, the hole was sealed with a screw to avoid exposure of the sample to the outer atmosphere. Before performing XAS analysis, the sample was purged with N_2 gas for 30 min to eliminate volatile compounds. Subsequently, it was reduced with 10 % H_2 at 300 °C for 1 h to remove oxides. An annealing temperature of 300 °C was not high enough to change the solid features dramatically. This was supported by XAS and TEM measurements, in which no obvious change in coordination number and particle size was observed, respectively. The total amount of sample was adjusted to reach the optimum absorption thickness ($\Delta\mu x = 1.0$, in which $\Delta\mu$ is the absorption edge, x is the thickness of the sample) so that a proper edge jump step could be achieved during the measurements. All spectra were recorded at room temperature in the transmission mode. Higher harmonics were eliminated by detuning the double-crystal Si(111) monochromator. Three gas-filled ionization chambers were used in series to measure the intensities of the incident beam (I_0), the beam transmitted by the sample (I_t), and the beam subsequently transmitted by the reference foil (I_r). The third ion chamber was used in conjunction with the reference sample, a Pt foil for the Pt L_{III}-edge measurements, and a Co foil for Co K-edge measurements. All measurements were compared against those for the reference samples. The control of parameters for EXAFS measurements, data collection modes, and calculation of errors were performed following the guidelines of the International XAFS Society Standards and Criteria Committee and processed by standard procedures.[41]

EXAFS data analysis: The EXAFS function χ was obtained by subtracting the post-edge background from the overall absorption and then normalized with respect to the edge jump step. The normalized χ (E) was transformed from energy space to k-space, in which "k" is the photoelectron wave vector. The $\chi(k)$ data were multiplied by k^2 to compensate for the damping of EXAFS oscillations in the high k-space. Subsequently, k^2-weighted $\chi(k)$ data in k-space ranging from 3.53 to 13.95 $Å^{-1}$ for the Pt L_{III}-edge and from 3.53 to 10.36 $Å^{-1}$ for the Co K-edge were transformed to r-space by Fourier transform to separate the EXAFS contributions from different coordination shells. A nonlinear least-squares algorithm was applied to the curve fitting of an EXAFS in the r-space between 1.8 and 3.2 Å for both Pt and Co, depending on the bond(s) to be fitted. The Pt–Co reference file was calculated based on theoretical considerations. Reference phase and amplitude for the Pt–Pt absorber–scatterer pairs were obtained from a Pt foil. Likewise, this was applied to a Co foil. All the computer programs were implemented in the UWXAFS 3.0 package[42] with the backscattering amplitude and the phase shift for the specific atom pairs calculated by the FEFF7 code.[43] From these analyses structural parameters, such as coordination number (N), bond length (R), a mean-squared disorder for the bond distance (σ^2_j), and inner potential shift (ΔE_0), were calculated. The amplitude reduction factor S_0^2 for the Pt and Co was obtained from Pt and Co foil reference samples by fixing the coordination number in the FEFFIT input file. The S_0^2 values were found to be 0.95 and 0.72 for Pt and Co, respectively.

Electrode preparation and electrochemical measurements: Millipore water (18 MΩ) and sulfuric acid (Acros) were used throughout the study. All the experiments were carried out at an ambient temperature of 25 ± 1 °C. A conventional electrochemical cell with three-electrode setup was used for cyclic voltammetry measurements, with a high-surface-area Pt counter electrode and a saturated calomel electrode (SCE) reference, powered by a Solartron 1480 potentiostat/galvanostat. The working electrode was made of the carbon-supported Pt–Co catalyst nanoparticles immobilized on a glassy carbon electrode (GCE) surface (0.1964 cm^2). The electrode was prepared by dispersing a known amount of Pt–Co/C in a Nafion™ solution (0.5 wt %) with an ultrasonic bath. Consequently, the suspension (7 μL, approximately containing 43.2 μg of Pt) was coated on the GCE disc. The GCE disc was left to air-dry for about 5 min at room temperature and then kept in an oven at 80 °C to uniformly produce a thin-film catalyst. A 0.5 M sulfuric acid solution was used as the supporting electrolyte for all the measurements. All potentials are quoted herein with respect to the RHE.

Acknowledgements

The authors gratefully acknowledge the financial support from the National Science Council (NSC-98-2120M-011-001 and NSC-97-2221-E-011-075-MY3), and facilities from the National Synchrotron Radiation Research Center (NSRRC) and the National Taiwan University of Science and Technology.

---

[1] *Advanced Electrochemical Science and Engineering* (Eds.: S. Gottesfeld, T. A. Zawodzinski, R. C. Alkire, D. M. Geroscher, D. M. Kolb, C. W. Tobias), Wiley-VCH, Weinheim, **1997**, pp. 195–209.
[2] M. Winter, R. Brodd, *Chem. Rev.* **2004**, *104*, 4245.
[3] Q. Li, R. He, J. O. Jensen, N. J. Bjerrum, *Chem. Mater.* **2003**, *15*, 4896.
[4] H. A. Gasteiger, S. S. Kocha, B. Sompalli, F. T. Wagner, *Appl. Catal. B* **2005**, *56*, 9.
[5] J. L. Fernandez, A. J. Bard, *Anal. Chem.* **2003**, *75*, 2967.
[6] B. J. Hwang, S. M. S. Kumar, C. H. Chen, Monalisa, M. Y. Cheng, D. G. Liu, J. F. Lee, *J. Phys. Chem. C* **2007**, *111*, 15267.
[7] F. H. B. Lima, E. A. Ticianelli, *Electrochim. Acta* **2004**, *49*, 4091.
[8] S. Mukerjee, S. Srinivasan, M. P. Soriaga, *J. Phys. Chem.* **1995**, *99*, 4577.
[9] F. J. Lucazk, D. A. Landsman, U.S. Patent 4447506, **1984**.
[10] S. Mukerjee, S. Srinivasan, *J. Electroanal. Chem.* **1993**, *357*, 201.
[11] A. S. Aricò, A. K. Shukla, H. Kim, S. Park, M. Min, V. Antonucci, *Appl. Surf. Sci.* **2001**, *172*, 33.
[12] A. K. Shukla, M. Neergal, P. Bera, V. Jayaram, M. S. Hegde, *J. Electroanal. Chem.* **2001**, *504*, 111.
[13] Y. Xu, A. V. Ruban, M. Mavrikakis, *J. Am. Chem. Soc.* **2004**, *126*, 4717.
[14] M. Mavrikakis, B. Hammer, J. K. Nørskov, *Phys. Rev. Lett.* **1998**, *81*, 2819.
[15] M. Min, J. Cho, K. Cho, H. Kim, *Electrochim. Acta* **2000**, *45*, 4211.
[16] T. Toda, H. Igarashi, M. Watanabe, *J. Electrochem. Soc.* **1998**, *145*, 4185.
[17] T. Toda, H. Igarashi, H. Uchida, M. Watanabe, *J. Electrochem. Soc.* **1999**, *146*, 3750.
[18] J. Zhang, M. B. Vukmirovic, K. Sasaki, A. U. Nilekar, M. Mavrikakis, R. R. Adzic, *J. Am. Chem. Soc.* **2005**, *127*, 12480.
[19] V. R. Stamenkovic, B. Fowler, B. S. Mun, G. F. Wang, P. N. Ross, C. A. Lucas, N. M. Markovic, *Science* **2007**, *315*, 493.
[20] V. R. Stamenkovic, B. S. Mun, M. Arenz, K. J. J. Mayrhofer, C. A. Lucas, G. F. Wang, P. N. Ross, N. M. Markovic, *Nat. Mater.* **2007**, *6*, 241.
[21] V. R. Stamenkovic, B. S. Mun, K. J. J. Mayrhofer, P. N. Ross, N. M. Markovic, *J. Am. Chem. Soc.* **2006**, *128*, 8813.
[22] S. Koh, P. Strasser, *J. Am. Chem. Soc.* **2007**, *129*, 12624.
[23] S. Chen, W. Sheng, N. Yabuuchi, P. J. Ferreira, L. F. Allard, Y. S. Horn, *J. Phys. Chem. A* **2009**, *113*, 1109.
[24] S. C. Zignani, E. Antolini, E. R. Gonzalez, *J. Power Sources* **2008**, *182*, 83.
[25] L. M. Roen, C. H. Paik, T. D. Jarvi, *Electrochem. Solid-State Lett.* **2004**, *7*, A19.
[26] X. Yu, S. Ye, *J. Power Sources* **2007**, *172*, 145.
[27] M. Watanabe, K. Tsurumi, T. Mizukami, T. Nakamura, P. Stonehart, *J. Electrochem. Soc.* **1994**, *141*, 2659.
[28] P. J. Ferreira, G. J. la O', Y. Shao-Horn, D. Morgan, R. Makharia, S. Kocha, H. A. Gasteiger, *J. Electrochem. Soc.* **2005**, *152*, A2256.
[29] B. Lim, J. Wang, P. H. C. Camargo, M. Jiang, M. J. Kim, Y. Xia, *Nano Lett.* **2008**, *8*, 2535.
[30] F. R. Fan, D. Y. Liu, Y. F. Wu, S. Duan, Z. X. Xie, Z. Y. Jiang, Z. Q. Tian, *J. Am. Chem. Soc.* **2008**, *130*, 6949.
[31] D. Ferrer, A. Torres-Castro, X. Gao, S. Sepúlveda-Guzmán, *Nano Lett.* **2007**, *7*, 1701.
[32] B. J. Hwang, L. S. Sarma, J. M. Chen, C. H. Chen, S. C. Shih, G. R. Wang, D. G. Liu, J. F. Lee, M. T. Tang, *J. Am. Chem. Soc.* **2005**, *127*, 11140.
[33] B. J. Hwang, Y. W. Tsai, L. S. Sarma, C. H. Chen, J. F. Lee, H. H. Strehblow, *J. Phys. Chem. B* **2004**, *108*, 15096.
[34] P. H. Citrin, G. K. Wertheim, *Phys. Rev. B* **1983**, *27*, 317.
[35] G. Meitzner, G. H. Via, F. W. Lytle, J. H. Sinfelt, *J. Phys. Chem.* **1992**, *96*, 4960.
[36] A. N. Mansour, J. W. Cook, D. E. Sayers, *Chem. Phys.* **1984**, *88*, 2330.
[37] S. N. Reifsnyder, M. M. Otten, D. E. Sayers, H. H. Lamb, *J. Phys. Chem. B* **1997**, *101*, 4972.
[38] B. J. Hwang, S. M. S. Kumar, C. H. Chen, R. W. Chang, D. G. Liu, J. F. Lee, *J. Phys. Chem. C* **2008**, *112*, 2370.
[39] J. Erlebacher, M. J. Aziz, A. Karma, N. Dimitrov, K. Sieradzki, *Nature* **2001**, *410*, 450.
[40] B. J. Hwang, L. S. Sarma, G. R. Wang, C. H. Chen, D. G. Liu, H. S. Sheu, J. F. Lee, *Chem. Eur. J.* **2007**, *13*, 6255.
[41] a) See, for example, the guidelines for data collection modes for EXAFS measurements and user-controlled parameters: http://www.i-x-s.org/OLD/subcommittee_reports/sc/SC00report.pdf;

b) See, for example, the guidelines for error reporting: http://www.i-x-s.org/OLD/subcommittee_reports/sc/err-rep.pdf.

[42] E. A. Stern, M. Newville, B. Ravel, Y. Yacoby, D. Haskel, *Physica B + C* **1995**, *208–209*, 117.

[43] S. I. Zabinski, J. J. Rehr, A. Ankudinov, R. C. Albers, M. Eller, *J. Phys. Rev. B* **1995**, *52*, 2995.

Received: August 14, 2009
Revised: January 23, 2010